A 2-D PIC/MC/Vlasov method for electrostatic fusion discharges

M. Fitzgerald [a,*], J. Khachan [b]

[a] *Research School of Physical Sciences and Engineering, Australian National University, 0200 ACT, Australia*
[b] *School of Physics, University of Sydney, Sydney 2006, Australia*

ARTICLE INFO

ABSTRACT

A kinetic plasma simulation is presented for an Electrostatic Fusion device operating at units and tens of mTorr. The simulation included particle-in-cell (PIC), Monte Carlo (MC) and Vlasov equation components. The simulation was designed to model these devices including previously neglected atomic physics interactions and to subsequently generate experimental Doppler spectra for verification. The large variation in plasma conditions in the different regions of these devices required a number of different mitigating techniques. A novel kinetic treatment of cold electrons is presented.

1. Introduction

Inertial Electrostatic Confinement (IEC) devices produce nuclear fusion reactions in relatively small and simple experiments. Gridded IEC devices consist of concentric semi-transparent electrodes under vacuum in the presence of ions [1–3]. Systems where an inner cathode is surrounded by an outer spherically or cylindrically symmetric anode have been of interest. The ions (typically Deuterium) are the fuel for fusion reactions when they are accelerated to energies of units and tens of keV, where the fusion cross-section becomes significant. The transport behavior of fast ions in these gridded IEC devices, operating at pressures of units and tens of mTorr, is a matter of some dispute [4], with evidence for a significant positive space charge accumulating at the center of the cathode [5–8]. The search for the mechanism behind the formation of this 'virtual anode' leads to basic questions about the role of cold discharge processes in the physics of IEC; Is the space charge formed by opposing cathode sheaths as seen in the hollow cathode effect? How important are ion creation processes to the formation of space charge?

A significant body of experimental evidence exists on the Doppler emission spectra of these devices with varying degrees of certainty in their interpretation [8–12]. In this paper we present a kinetic plasma simulation which includes a number of relevant cold cathode discharge processes and generates Doppler spectra for direct verification against this diagnostic. The Monte Carlo technique to generate these spectra will be presented as well as other cold discharge aspects of the simulation.

Some success with MC/PIC on IEC has been reported previously [13] for understanding self-sustaining discharges outside the cathode region. However, physical conditions at the center of the cathode vary greatly to the conditions outside the cathode, which poses difficulties to modeling this important region. Of particular concern is the accumulation of cold electrons in low field regions. A new approach which uses a Vlasov solver to model cold electron populations in the center will be discussed.

2. Particle-in-cell code limits

Experimentally obtained densities as well as evidence of space charge limited current behavior [6] suggested that the affect of charge density gradients on the total electric field needed to be included in the model. A particle-in-cell (PIC) code was implemented to simulate this. The PIC technique is a way of approximating the density of charges at discrete points in space so that the local electric field can then be calculated [14]. This is done by tracking a computationally manageable number of simulation superparticles with each representing a much larger number of real particles. The cumulative charge of each superparticle is assigned to nearby spatial grid points as a function of distance. A good review with recent advances can be found here [15].

* Corresponding author.
E-mail address: Michael.Fitzgerald@anu.edu.au (M. Fitzgerald).

The approximations of this technique make any such simulation susceptible to unphysical numerical instability if certain limitations are not respected [16]. An important limitation concerns the allowed coarseness of the spatial grid in regions where the Debye length for the simulated particles becomes comparable to the grid-point separation.

The approximations also force a compromise between simulations that conserve momentum or those that conserve energy, contingent on the procedure by which the electric field on the particle is calculated [14]. It has also been shown that energy conserving PIC codes are less susceptible to numerical instability caused by coarse spatial grids. The total momentum conservation of the simulated plasma was seen as less important for our purposes than its energy conservation because gridded IEC devices employ fixed electrodes that provide much of the impulse for the plasma particles.

The limitations on grid spacing and stability were of particular importance in the simulation of IEC devices. The energies and densities of ions and electrons were expected to vary significantly with distance from the cathode. The 'core' region at the center of IEC cathodes was anticipated to be problematic because of the large accumulation of cold electrons in a low field region. This implied that the Debye length for electrons in the core would be particularly short and thus difficult to resolve with the spatial grid.

A non-uniform spatial grid technique was used that reduced the grid separation in regions where the Debye length was expected to be short whilst reducing the number of grid points in less critical areas thus conserving overall computation resources. A 2-D energy conserving PIC algorithm was devised to add to the stability of the code and is described in Appendix A.

2.1. Cold electron Vlasov code

Computational constraints limit the number of simulated spatial grid points. Where the electron Debye length becomes shorter than 0.3 of the grid point separation, an unphysical numerical instability known as *grid heating* or *finite grid instability* can manifest itself in PIC codes. This translates into a statement about the minimum energy and maximum density of electrons in the discharge for a satisfactory model, two properties that were largely unknown experimentally. In the course of simulation, it became clear that in regions close to the cathode, calculated electron densities from created secondary electrons were responsible for large instabilities in electron energy, which in turn artificially increased the level of ionization to a point where the numerical solution diverged. The troublesome cold electrons were a significant contribution to the overall charge and could not have been neglected without intolerably violating charge conservation.

As with all the other simulated densities, the cold electron density is defined on the spatial grid domain used to solve the electrostatic potential. Where the simulated electron energy is too low, or the electron density too high, superparticles representing electrons must be transferred from the PIC component of the model in order to maintain stability. Electron density is computed using the usual PIC weighting method, and the nearest grid points to each electron are stored. Taking a pessimistic approach to the stability, the highest density computed of the four nearest points is used in the Debye length calculation. The Debye length for two degrees of velocity freedom and a kinetic energy, KE, is given by

$$\lambda_D = \sqrt{\left(\frac{\epsilon_0 KE}{e^2 n_e}\right)} \tag{1}$$

Again using the worst case, the maximum nearest grid spacing ΔX from Δr or Δz is chosen for the calculation. Consistent with the stability criterion of $0.3\Delta X < \lambda_D$, the minimum allowed kinetic energy for an electron is

$$KE_{\min} = \frac{(0.3\Delta X)^2 n_e e^2}{\epsilon_0} \tag{2}$$

At each time step, the simulation looks at every superelectron to see if it meets the corresponding minimum energy requirement, and if not, then the density contribution of that superelectron is added to the electron continuum density on the grid.

The particle simulation is a kinetic model, so the corresponding analytical expression is given by the Boltzmann equation

$$\frac{\partial f}{\partial t} + \vec{v} \cdot \vec{\nabla} f + \vec{a} \cdot \vec{\nabla}_v f = \frac{df}{dt}_{collisions} \tag{3}$$

where $\frac{df}{dt}_{collisions}$ describes the rate at which the probability density changes as a result of collisions. This can be decomposed into particle loss and creation terms which directly correspond to the processes described by the Monte Carlo model. The difficulty in solving Eq. (3) is the motivation for the Monte Carlo approach.

If we remove electrons from the MC/PIC component of the model, we lose the ability to model their collisions. Reproducing ionization rates is critical, so grid spacing is always chosen such that electrons above the ionization energy could be modeled by the MC/PIC code. Thus low energy collisions for cold electrons are neglected. The collisionless Boltzmann equation (alternately known as the Vlasov equation) is given by

$$\frac{\partial f}{\partial t} + \vec{v} \cdot \vec{\nabla} f + \vec{a} \cdot \vec{\nabla}_v f = 0 \tag{4}$$

When cold electrons are removed from the MC/PIC code, they are assigned to the density function $n_{e,cold}(r, z, v_r, v_z)$ on a 2-D spatial and 2-D velocity domain. The equation is solved each timestep by a 2nd order accurate interpolation method [17] repeated briefly here. For each spatial dimension, the equation is split into two equations which express stepping in position and velocity respectively. Using the fact that the probability density f multiplied by the average density gives $n_{e,cold}(r, z, v_r, v_z)$ we obtain (omitting subscripts on the density)

$$\frac{\partial n}{\partial t} + v_r \frac{\partial n}{\partial r} = 0 \tag{5}$$

$$\frac{\partial n}{\partial t} + v_z \frac{\partial n}{\partial z} = 0 \tag{6}$$

$$\frac{\partial n}{\partial t} + a_r \frac{\partial n}{\partial v_r} = 0 \tag{7}$$

$$\frac{\partial n}{\partial t} + a_z \frac{\partial n}{\partial v_z} = 0 \tag{8}$$

This splits the acceleration and translation steps of the numerical scheme, allowing a 'leap-frog' approach similar to that used for time integrating PIC codes. Explicitly for the r-axis

$$n*(r, z, v_r, v_z) = n\left(r - v_r\left(\frac{\Delta t}{2}\right), z, v_r, v_z\right)$$

$$n**(r, z, v_r, v_z) = n*\left(r, z, v_r - a_r(\Delta t), v_z\right)$$

$$n(r, z, v_r, v_z) = n**\left(r - v_r\left(\frac{\Delta t}{2}\right), z, v_r, v_z\right)$$

and similarly for the z-axis for each time iteration. The acceleration a_r is computed from the local electric field. In this simulation, the electric field is defined in between grid points not at the grid points, so the easiest approximation to the field at the node is the average of the two nearby edge values.

Although this technique faithfully evolves the relative number density in time, it was found that it doesn't conserve total number

of particles very well for coarse grids. To remedy this, the density is normalized to particle number for each timestep. Stated differently; the total probability is always normalized to one.

In other simulations, these cold electrons are typically treated as a fluid (see for example [18]). For typical low temperature collisional high pressure discharges, that hybrid approach is reasonable to describe thermal and energetic populations differently. However, at mTorr pressures, even the cold electrons are unlikely to be collision dominated. To the authors knowledge, this is the first purely kinetic treatment of cold continuum electrons in PIC simulation.

3. Monte Carlo code

A Monte Carlo component to the simulation was used to calculate rates of particle creation, loss and scattering. Monte Carlo simulation is a well-understood approach [19] for computing these rate parameters, thus only the unique aspects of this IEC simulation are presented here. Complete details of other collisions in the model may be found elsewhere [20].

3.1. Charge exchange: $H_2^+ + H_2 \Rightarrow H_2^+ + H + H^*$

For ion energies above 70 eV in hydrogen, charge exchange is the dominant process [21] and is a maximum at approximately 10 keV. This results in the creation of a slow ion and a fast neutral which later disassociates. Experimental evidence for energetic neutrals dominating the Doppler emission spectra obtained from any IEC device suggests the importance of this interaction [4]. Much has been deduced from interpreting these spectra and modeling charge exchange alone [10].

The Monte Carlo interaction is straightforward; create a new energetic neutral with the same incoming momentum, and then set the incoming ion momentum to be the cold background gas temperature. The neutral will be created with an outer electron in an excited state.

At some time after the creation of the neutral it will disassociate into two neutral hydrogen atoms, one of which will be excited. At some time after that, the excited fast neutral will decay producing a photon. Modeling this decay lifetime is important to explain the directionality and origin of neutrals responsible for the Doppler spectra. A Monte Carlo approach to simulate a correct lifetime for the excited neutral is to assign a random lifetime to each created neutral based on the expected distribution of lifetimes. To take advantage of the existing experimental data, H_α is the transition of interest, so we assume that the molecular ion disassociates immediately and the electron starts in the principle quantum number $n = 3$ excited state. The transition rate for the observed decay is given by the accepted Einstein coefficient for the transition $A_{3 \to 2}$ [22], but this does not take into account other possible de-excitation routes. A more dominant decay is $A_{3 \to 1}$ which is an order of magnitude more frequent (Table 1). The expected number of excited atoms N at time t is given by a decaying exponential as

$$N_{n=3}(t) = N_{n=3}(0)e^{-(A_{3 \to 2} + A_{3 \to 1})t} \tag{9}$$

which implies that we can assign a random lifetime for each new excited neutral as

$$t(RN) = -\frac{1}{(A_{3 \to 2} + A_{3 \to 1})} \ln(RN) \tag{10}$$

where RN represents a random number from the interval $(0, 1]$. The lifetime counter for each individual fast neutral superparticle is decremented at each time step until it reaches zero, when the neutral is no longer considered visible.

Table 1
De-excitation rates associated with the $n = 3$ state of atomic hydrogen.

A_n	Configuration	Rates (s^{-1})
$A_{3 \to 1}$	3p–1s	1.672e+08
	3p–1s	1.672e+08
$A_{3 \to 2}$	3p–2s	2.245e+07
	3s–2p	2.104e+06
	3p–2s	2.245e+07

Artificially assuming that every excited neutral is created in the $n = 3$ state will over-estimate the total power radiated for the transition, but we are not concerned with the power of the H_α emission but rather over what distance the neutral population represented by the superparticle can possibly be expected to still be excited and therefore able to emit. The number of superparticle neutrals at any given timestep is a fraction of the number of ions, determined by the charge-exchange probability per timestep. Although much slower than electrons, the neutrals are only relevant over the period of timesteps that they are still considered in an excited quantum state, which is much shorter than their confinement time. Thus we again have the problem of noisy statistics. A further requirement is that the generated distribution functions are spatially dependent, thus all existing neutrals would have to be 'binned' by location, reducing the number per bin and increasing the noise.

The solution was to perform a summation of emission rate over the duration of the simulation, thus obtaining an average emission. Emission spectra are obtained experimentally by collecting photons over timescales well beyond those simulated making this approach sensible not just necessary.

The generated spectra could include emission contributions from when the simulation was still evolving to an equilibrium, or it could use a shorter time window to only include later emission, so as to more faithfully reproduce an equilibrium spectrum. A larger window means less statistical noise but more transient effects. That isn't to say that transient effects are unphysical, rather that spectra collected in a pulsed mode would be a more rigorous test for a simulation that starts from vacuum.

3.2. Photoelectrons: $\gamma \Rightarrow e^-$

It has been suggested that the photoelectric effect plays a role in hollow cathode discharges [23]. Spontaneous emission ending in the ground state will result in a hard ultraviolet photon being emitted, with an energy well above the 4 eV work function of stainless steel [24]. Electrons with tens of electron volts would then be released from any metallic surfaces depending on illumination.

To simulate this process in detail, a full collisional-radiative model would need to be created to calculate radiated power output at interesting photon wavelengths. Some sort of ray tracing code would then need to deduce the received power on the cathode to decide where and in what quantities electrons need to be ejected. This was well beyond the scope of this simulation. For simple geometries, there are a number of approximations that provide an upper limit on the cathode photoelectric current.

The radiant power of the plasma is a function of how much of the plasma is excited. Ionization from the ground state is an excitation process comparable in energy to the ultraviolet emission lines of hydrogen, so one could expect that the density of excited atoms would be less than the density of ions, especially if the incident exciting particles have energies greater than the ionization energy. Emission due to recombination would also be absolutely limited by the density of ions. So the number density of ions provides an excited neutral number density upper limit. A number of

Table 2
De-excitation rates producing photons energetic enough to create photoelectron emission from the cathode.

Energy (eV)	Configuration	Rate (s^{-1})
10.1988057	2p–1s	6.265e+08
10.1988511	2p–1s	6.265e+08
12.0874931	3p–1s	1.672e+08
12.0875066	3p–1s	1.672e+08
12.7485319	4p–1s	6.818e+07
12.7485375	4p–1s	6.818e+07
13.0544976	5p–1s	3.437e+07

different transitions to ground state in hydrogen produce energetic enough photons for photoelectron production [22]. Fermi statistics requires that lower electron energy levels are more likely to be populated than higher energy levels, and to be completely rigorous, we would set the population at each excited level accordingly and deduce the emission rate by taking an average. Given that we have already assumed that no electrons exist at the ground state for our excited population, we can set an upper limit on the photo emission rate by choosing the energy level with the highest transition rate to hold our entire population. Therefore the rate of photon emission is limited by the 2p–1s transition rate (Table 2). For the hollow cathode effect, we are mostly concerned with the electron production rate inside the cathode. Given the high visible emission in the center, it is not unreasonable to take the radiating volume to be that enclosed by the cathode (approximately a cylinder for the biconical cathode case). The illuminated surface then becomes the inner surface of the cathode. The number of photoelectrons emitted by the inner surface depends on the number of incident photons multiplied by the quantum efficiency for the metal. As an upper limit, this is taken as 100%. When multiplied over the time step, the rate becomes an absolute number of electrons created in that time step. If the number of electrons is at least comparable to the typical super particle size ξ, then superparticles are released at random points on the inner surface of the electrode with the maximum possible energy of 6 eV, which is the energy of the incoming photon minus the work function.

3.3. Secondary electrons and other surface effects

A key process in any glow discharge phenomenon is the creation of electrons at the cathode due to positive ion bombardment. The Monte Carlo simulation of secondary electrons is straightforward; decide if an ion impacts with the cathode, look up the probability of electron creation based on the ion kinetic energy on impact, then generate a random number. Destroy the ion, and create an electron depending on the outcome of the random number. A created electron will contribute to the current calculated for the given time iteration.

Raizer [25] gives an empirical formula for the secondary electron yield $\gamma = 0.016(I - 2e\psi)$ eV which is correct to 50% (I is the incident ion energy and ψ is the work function). Given the similarities in work function between copper and steel (4.4 eV and 4.31 eV respectively), experimental values for the secondary yield of copper [24] were used instead, which should be much closer than 50% to the yield for stainless steel.

Regardless of whether ions impacting on the cathode result in a secondary electron or not, ions will be reflected or lost according to experimental rate coefficients [26,27]. For simplicity, reflected ions are assumed to rebound elastically due to a force normal to the surface. Ions that are not reflected are considered lost and contribute to the current for the given time iteration. It is assumed that ions are backscattered with the incident energy.

3.4. Coalescing and splitting PIC particles in high or low field IEC regions and the resulting statistics 'theft'

It was expected that electron and ion densities were significantly different near the IEC cathode. This meant that if the electron and ion densities were to be calculated with an equal number of superparticles, then the number of particles represented by superelectrons needed to be different to the corresponding weighting for super-ions.

The problem in using differing superparticle sizes arises when an electron creates an ion or vice versa. For example, consider a single real electron ionizing the background gas producing a single electron and ion. If a superelectron is to simulate this interaction correctly, then it must produce a superelectron and superion of the same size, otherwise the total charge before the interaction will not be conserved after the reaction. The solution used here was to assign sizes on a per particle basis, rather than on a per species basis. Thus each superparticle had its own individual position, momentum and size.

The number of particles represented by each superparticle was rescaled during the course of the simulation. Approaches exist [28] for coalescing or splitting particles when the number in any given cell is outside a prescribed boundary, however differences in field strength between inside and outside the cathode implied that such a local rescaling approach could not be consistently applied. In high field regions outside the cathode, short electron transit timescales and low electron creation rates meant that these cells were often free of particles. Thus a global particle number approach was taken.

Upper and lower bounds for the global number of simulation particles in each species were defined and an algorithm monitored actual numbers with each iteration. If the number of macro particles went below a set amount, then each particle was duplicated and the weighting was halved. There are subtleties to the way this is global approach needs to be done that do not seem to be mentioned in the literature, probably because particle sizes are usually kept the same across species.

Supposing, for example, that the number of electrons in the simulation decreases below the prescribed minimum. All electrons remaining in the simulation would be duplicated and their sizes halved. As fast electrons leave the simulation faster than slow electrons, this tends to skew the distribution function towards cold electrons, which describes an evaporative cooling effect and is physically sensible. However, supposing there are stagnation points in the simulation where electrons have low energy and the local field is weak. This would mean that the low energy electrons would undergo many duplications with little prospect of promotion to becoming a contributing member of the simulation. Each time this occurs, their size would reduce making them less and less relevant to the simulation but instead taking the place of a more significant particle. Worse still, suppose an avalanche process in some other part of the plasma were to take place. If the avalanche increased the number of particles in the simulation past the upper limit prescribed, then all particles would be reduced in number without prejudice. This would reduce the statistics in the avalanche process when there were still plenty of insignificant electrons that could have been used instead. These insignificant electrons can also ionize and create even more stagnant ions. This 'statistics theft' effect was particularly problematic when modeling cathodes which are hollow, with a large field free region at the center (for vacuum solutions or solutions where the plasma wasn't yet sufficiently ionized).

A global solution to this problem which does not introduce a selection bias or violate charge conservation is not obvious. A compromise reached in this case was to look at the entire number of superparticles and re-scale only to keep the total number within
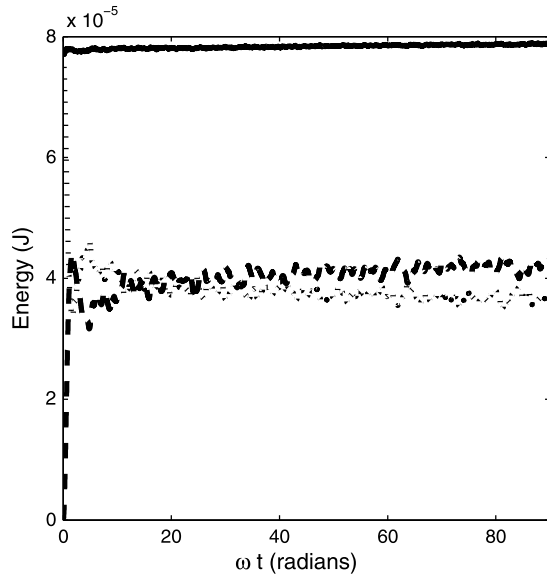
Fig. 1. Results of the energy conservation test. Dotted, dashed and solid lines represent the field, kinetic and total energies respectively. Field (kinetic) energy is maximum (minimum) at the start when the electrons are stationary.

Fig. 2. Kinetic (dashed) and field (dotted) energy contributions for the Langmuir wave benchmark using the lowest spatial Fourier mode $\sin(2\pi x/L)$. The total energy (solid) is also shown.

the limits, rather than any species individually. Regardless of any stagnant electrons, there would also be plenty of ions to keep the superparticle number high enough so that the re-scale algorithm is not triggered. This is quite appropriate in one sense because in a glow discharge dominated by secondary electrons the electron creation is limited by the ion impact rate on the cathode. In another sense this compromise guarantees that the number of electrons in the simulation at any given time will be a fraction of the number of ions and therefore produce noisier distributions. However, the key advantage of this method is that when an avalanche happens, the multiplication process is not stifled.

4. Results

4.1. Energy conservation

A scenario was constructed which consisted of a uniform distribution of superelectrons in the absence of electrodes. Electrons were never created or destroyed, but were instead reflected elastically at the boundaries of the simulation. The uniform density was chosen high enough such that the total mutual repulsion produced an initial potential of around -4 kV, corresponding to the sorts of electron energies expected in later IEC simulation. The superelectrons were evenly distributed along the grid, which meant that they had varying size as a function of radial starting position. The kinetic energy and electrostatic potential energy were calculated for the duration of the simulation. The simulation potential energy was taken as

$$PE = \frac{1}{2}\sum_{n=1}^{N} Q_n V_n \qquad (11)$$

where Q_n is the charge on node n and V_n is the corresponding electrostatic potential. The total kinetic energy was taken as the sum of the kinetic energies of each of the superparticles. The simulation was run over hundreds of plasma frequency oscillation periods ωt and the results are given in Fig. 1. The simulation scenario utilized a cold start, that is, all electrons started with zero velocity. The electrostatic potential energy is rapidly converted into kinetic energy, minimizing the action functional of the system as expected. The total energy of the simulation is very uniform, exhibiting an
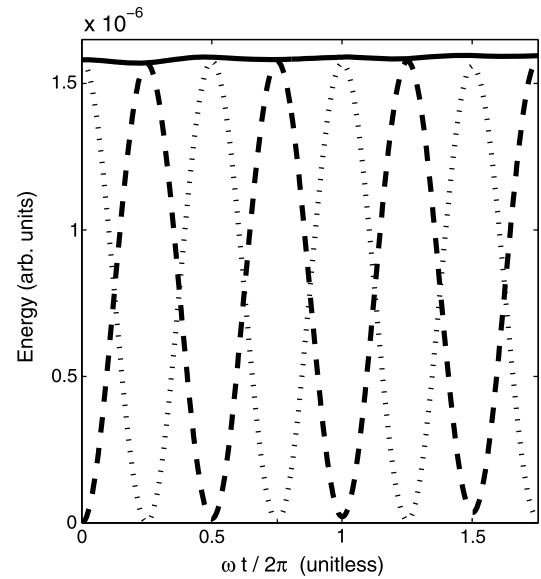
unphysical average growth of 1% over $\omega t = 90$. Whereas Okuda [16] finds that the 1-D Lewis code conserves energy to one part in 10^5, we found that this 2-D code had an almost identical unphysical energy growth rate to the force-interpolating momentum code under the same conditions even as time step was reduced (not shown). What is supposed to distinguish energy-conserving codes from momentum-conserving codes is the property that a shorter timestep results in better energy conservation in the former and not in the latter beyond some limit. However, Langdon [29] has expressed skepticism for achieving this in practice, stating that increased noise from using a lower order approximation diminishes any benefit. Work needs to be done to understand the energy-conserving properties of a 2-D cylindrical system, but the simulation stability was ample for our purposes.

4.2. Cold plasma wave test of the coupled Vlasov–PIC system

A 1-D periodic system was constructed to test the behavior of the coupled PIC and Vlasov approaches against the well-understood Langmuir wave solution; a repeat of a benchmark done for the PIC code ES1 [14]. The periodic simulation was constructed such that half the system was represented with the Vlasov model and the other half was represented with the PIC model. Ions were taken as immovable and distributed uniformly, and the initial locations of cold electrons were perturbed proportional to $\sin(2\pi nx/L)$ for various spatial mode numbers n. No smoothing or normalization of the distribution function or potential was performed during the tests. The kinetic energy of the Vlasov component was computed using a numerical double integral with the trapezoidal rule. The results for the first non-trivial spatial mode number are given in Figs. 2 and 3. The coupled Vlasov–PIC model reproduced the plasma frequency correctly with no dispersion with increasing mode number. No aliasing of the plasma frequency due to finite particle size [14] was observed, which is consistent with predictions for the energy-conserving PIC scheme used. The phase plot in Fig. 3 shows spurious broadening of the distribution function comparable to that normally encountered for the Vlasov only model [17]. A new feature of the coupled system is evident at the two junctions between regions of high PIC particle density and high Vlasov density. This appears to be caused by fluctuation in the electric field from a finite number of PIC particles. Since the Vlasov
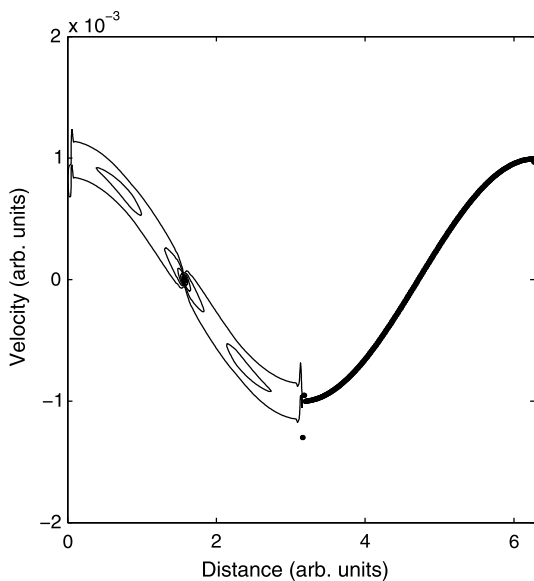
Fig. 3. Phase space for the Langmuir wave benchmark using the lowest spatial Fourier mode $\sin(2\pi x/L)$ after 1.75 plasma periods. The left side of the plot shows contours of constant probability distribution from the Vlasov model, and the right side shows the location of super particles from the PIC model in the coupled system.

step is very sensitive to the electric field, the fluctuating field causes filamention of the probability distribution function and further broadening of the particles in phase space. The increase that this has on total energy scales linearly with time and is reduced by increasing grid and particle number. No other numerical instability is observed as long as the distribution function goes to zero at the velocity limits of the phase space.

We expect that the strongly coupled and periodic benchmark presented here to be a more demanding numerical problem than the IEC case where the field is dominated by the applied potential and the PIC and Vlasov models are weakly interacting.

4.3. Validity of charge exchange Monte Carlo code

An important consideration in generating Doppler spectra is the decay of intensity with distance of the excited energetic neutrals. The decay of an excited population with a certain time-constant τ is described by a decaying exponential. For a given velocity v, the exponential relation is

$$N_{n=3}(x) = N_{n=3}(0)e^{-x/vt} \tag{12}$$

where $N_{n=3}(x)$ represents the number of atoms still in the excited state at a distance x. Although superficially reasonable, the procedure of assigning random lifetimes should be tested for convergence, especially considering that the sizes of Monte Carlo particles are allowed to vary in the model. A short test simulation was constructed; particles were started at the origin and given the same velocity and a random lifetime as described previously in Section 3.1. The particles were given random sizes between 1 and 20 000. The results are given in Fig. 4.

Note that the exponential decay function (and the simulation) describes the number of particles still excited after a certain distance traveled. Of course, what is observed by a spectrometer is the decay of particles, not the population still excited. Therefore, what is of interest here is the derivative of the excited population with space. Conveniently, the derivative of an exponential decay is also an exponential decay. Thus the observed intensity is correctly modeled by an exponential, which the model reproduces.
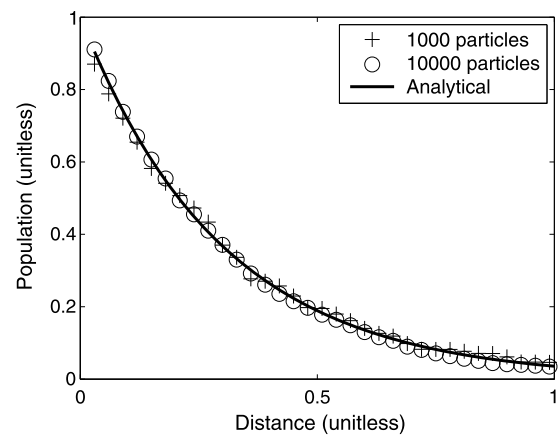

Fig. 4. Convergence simulation results for the Doppler shift Monte Carlo code.

Another concern for this modeling lies with the time constant of the decaying exponential. As mentioned earlier (Section 3.1), the lifetime of the $n = 3$ state is substantially shortened by the ultraviolet Lyman $3p \rightarrow 1s$ transition giving a mean lifetime of 5 ns. A previous study [30] (and others citing it) stated that the excited population is controlled by the 3s level half-life of 165 ns, which implies a time constant of $165/\ln(2) = 238$ ns. Obviously different to the 5 ns time constant proposed here, but also exactly half the NIST [22] value for the time constant of $1/(2.104 \times 10^6) = 475$ ns.

That confusion aside, the possibility exists that a proportion of fast neutrals are re-excited long after decaying by an intermediate process. Truly the most accurate way to understand the spatial excitation profile is with a collisional-radiative model which is too exhaustive for the purposes here (and those used successfully in practice as a tokamak diagnostic [30]). Nevertheless, what matters here is that an upper bound for the excited lifetime is used to discount fast neutrals being visible over a large distance as the primary explanation of the blue shifted spectra. Therefore, the longest conceivable lifetime of 475 ns was used, which for a 5 keV ion is 47 cm and well beyond the apparatus dimensions. Considering the exponential decay, and the fact that the ions didn't reach full energy in experiment, the decay as a function of distance was still included for generating the spectra.

A last consideration deals with the number of species being modeled. The kinetic model only contains H_2^+ reactions from the three hydrogenic ion charge exchange processes. This means that any change in concentration of species along the beam is ignored. For comparison with experiment, all spectra generated by the model include contributions from H^+ and H_3^+ by assuming the different species share the same energy, as has been shown [9,11]. The intensity ratios are taken from the visible peak heights in experimental spectra. Although this will be correct at maximum shifts, the heights will be wrong at shorter shifts because of the variation in charge-exchange cross-section for the three processes. The typical $H^+ : H_2^+ : H_3^+$ height ratio used was $1 : 2 : 5$.

4.4. Solution of Poisson's equation and overall particle behavior

The gridded IEC device given particular attention in this study utilized a cylindrically symmetric cathode at the center of a spherical anode. The cathode consisted of two hollow stainless steel cones attached base-to-base with an aperture along the axis. This 'biconical' cathode system was used in previous studies which identified anomalous ion transport behavior and was an important system to simulate. Tests of the electric field solution and particle behavior aspects of the model were performed on this electrode configuration. The simulated electrodes and discrete spatial grid
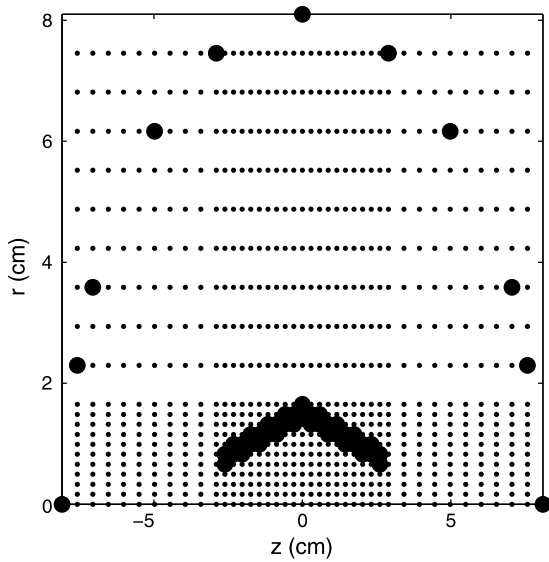
Fig. 5. Non-uniform spatial grid and electrode geometry for the full discharge simulation. Large dots near the center denote cathode points and the 11 large outer dots denote anode points.
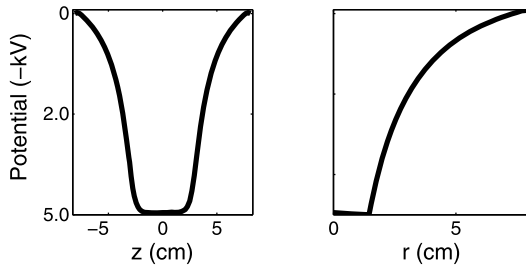

Fig. 6. Electrostatic potential at the end of the ion focus simulation. The left graph gives potential variation axially along $R = 0$ and the right graph gives the radial variation for the smallest Z value cross-section.

are shown for this 2-D cylindrically symmetric system in Fig. 5. The most basic IEC theory says that these devices focus ions inwards with symmetric potential wells where the ions fuse or are eventually lost to the semi-transparent cathode. An ion-only simulation without atomic Monte Carlo interactions was configured to both demonstrate this behavior as well as test aspects of the code; sensible results under these conditions re-enforce that the solution of the electrostatic potential on the non-uniform spatial grid and the particle dynamics are both correct. The coarse and non-uniform grid depicted in Fig. 5 was used in some of the ion focus simulations. A similarly coarse, but uniform, grid was also used for comparison. These grids were several times more course than what was used for later simulations which included electrons and the full atomic physics. The resulting solution of the electrostatic potential given in Fig. 6 closely matches the expected vacuum solution for the simpler concentric radially symmetric case. No distortion between uniform and non-uniform spatial grid solutions was observed. Some space charge distortion occurred where the ions were created near the anode. The ion focus scenario was repeated for different values of cathode voltage and for two different external ion creation rates, to obtain the steady-state current under different conditions. Fig. 7 shows the resulting V–I characteristic as predicted by the model. Features of the classic thermionic emission vacuum tube V–I curves are apparent, with a power law relationship at low values of applied voltage, and a saturation of current for high voltages which depended on the charge particle creation rate [31].
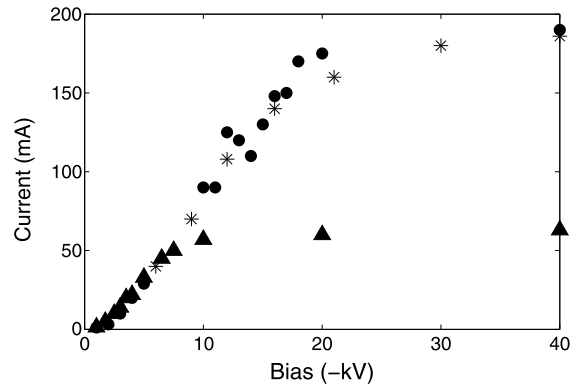

Fig. 7. Simulated V–I characteristic for the biconical cathode ion focus. The curves were generated by taking the steady-state current at the end of different simulation runs. The triangle and circle curves were produced with external ion production rates of 3×10^{17} cm^{-3} s^{-1} and 9×10^{17} cm^{-3} s^{-1} respectively on a uniform spatial grid. The stars represent the same conditions as the circle data but were computed using a non-uniform spatial grid.

The saturation level gave a threefold increase in maximum current for a threefold increase in ion creation rate as expected. This was due to the local electric field being dominated by the applied field, which resulted in all ions being accelerated by the applied field at the same rate.

Performing an estimate for the expected saturation current is straightforward. The external rate was set at 3×10^{17} cm^{-3} s^{-1}. The external rate was in terms of number density, not number, so that the ion density in simulation was uniform. The average cell volume for points along the anode interior is 1.33 cm^3 (this may seem large, but it includes the full 2π radians of a cell). This is where the ions were created. Thus the saturation current should approximately be 3.00×10^{17} cm^{-3} s^{-1} $\times$ 1.33 cm^3 $\times$ 1.60 $\times$ 10^{-19} C $= 63.9$ mA. Three times that value is 192 mA. These estimates match the values of saturation in Fig. 7.

A handful of simulations were performed using a non-uniform spatial grid which are also presented in Fig. 7. Very good agreement with the V–I characteristic was observed, with all but one point lying on the center of the trend. It is clear that the same physics was reproduced for both the uniform and non-uniform grids.

These results match previous experiments [6] and have important ramifications for the existing IEC theory which will be the subject of our next paper. For our purposes here, we can be confident in our field solutions and particle motion.

5. Conclusion

A kinetic model was constructed which incorporated PIC, Monte Carlo and Vlasov components. Problems which are characteristic of, but not unique to, IEC modeling were presented and a number of new techniques were described.

Differing ion and electron densities were dealt with by allowing superions and superelectrons to have different weightings, and the resulting problems on MC statistics were managed. Low field regions and the resulting cold electrons were treated using a non-uniform grid, Vlasov code and 2-D energy conserving code. The energy conserving code and the non-uniform grid solver were both tested and shown to produce physical results.

The role of the cathode surface in creating electrons through secondary emission and photoionization was incorporated into a Monte Carlo code. Doppler emission spectra were created using a Monte Carlo technique where excited neutrals were given random lifetimes. This allowed for contributions to the emission spectra from energetic neutrals in transit. The Doppler emission Monte

Carlo code was tested against the theoretical exponential decay with distance and was found to be correct.

More standard aspects of the code were not presented here and the details of which can be found elsewhere [20] including a list of all simulated MC interactions. The full results of this modeling of mTorr IEC will be the subject of a future publication.

Acknowledgements

Appendix A

A.1. Non-uniform grid

The PIC method relies on a discrete solution of Poisson's equation

$$\vec{\nabla}^2 V(\vec{x}) = -\frac{\rho(\vec{x})}{\epsilon_0} \tag{13}$$

To obtain a discrete version of Eq. (13), we need to expand the spatial derivatives in terms of neighboring points [32].

$$V(x+dx, y, z) \approx V(x, y, z) + dx\frac{\partial V}{\partial x} + \frac{1}{2}dx^2\frac{\partial^2 V}{\partial x^2} \tag{14}$$

$$V(x-dx, y, z) \approx V(x, y, z) - dx\frac{\partial V}{\partial x} + \frac{1}{2}dx^2\frac{\partial^2 V}{\partial x^2} \tag{15}$$

Adding Eqs. (14) and (15) and rearranging gives an expression for the second derivative, with an identical derivation for the remaining dimensions y and z.

$$\frac{\partial^2 V}{\partial x^2} \approx \frac{V(x+dx, y, z) + V(x-dx, y, z)}{dx^2} - \frac{2V(x, y, z)}{dx^2} \tag{16}$$

Replacing derivatives in Eq. (13) with (16) gives the discrete Poisson equation for a uniform grid.

$$\sum_{X=x,y,z} \frac{V(+dX) + V(-dX) - 2V(\vec{x})}{dX^2} = -\frac{\rho(\vec{x})}{\epsilon_0} \tag{17}$$

Eq. (17) defines a set of N coupled linear equations for N grid points. This is the typical system of equations that is solved by matrix inversion or relaxation for a uniform grid.

For a non-uniform grid, a problem only arises when considering the derivative on the border between regions of different grid coarseness. We proceed by expanding the derivative in a more general way where the separation between points forwards dx_+ is not necessarily the same as dx_-, the separation backwards.

$$V(x+dx_+, y, z) \approx V(x, y, z) + dx_+\frac{\partial V}{\partial x} + \frac{1}{2}dx_+^2\frac{\partial^2 V}{\partial x^2} \tag{18}$$

$$V(x-dx_-, y, z) \approx V(x, y, z) - dx_-\frac{\partial V}{\partial x} + \frac{1}{2}dx_-^2\frac{\partial^2 V}{\partial x^2} \tag{19}$$

These two equations are then used to obtain an expression for the derivative and the corresponding discretization of Poisson's equation (21).

$$\frac{\partial^2 V}{\partial x^2} \approx \frac{2V(x+dx_+, y, z)}{dx_+dx_- + dx_+^2} - \frac{2V(x, y, z)(1+\frac{dx_+}{dx_-})}{dx_+dx_- + dx_+^2}$$
$$+ \frac{2(\frac{dx_+}{dx_-})V(x-dx_-, y, z)}{dx_+dx_- + dx_+^2} \tag{20}$$

$$\sum_{X=x,y,z}\left(\frac{2V(+dX_+)}{dX_+dX_- + dX_+^2} + \frac{2V(-dX_-)(\frac{dX_+}{dX_-})}{dX_+dX_- + dX_+^2}\right.$$
$$\left. - \frac{2V(\vec{x})(1+\frac{dX_+}{dX_-})}{dX_+dX_- + dX_+^2}\right) = -\frac{\rho(\vec{x})}{\epsilon_0} \tag{21}$$

Dirichlet boundary conditions are specified by setting the unknown potential at chosen points $V(\vec{x})$ equal to the required potential $V_0(\vec{x})$, reducing the number of unknowns.

Experiments in cylindrically symmetric IEC for units and tens of mTorr pressure ranges have similar physics to those with spherically symmetric electrodes and were of interest in this study. This reduced the dimensionality and number of grid points required in simulation for a given resolution. Poisson's equation becomes

$$\frac{\partial^2 V}{\partial r^2} + \frac{1}{r}\frac{\partial V}{\partial r} + \frac{\partial^2 V}{\partial z^2} = -\frac{\rho(r, z)}{\epsilon_0} \tag{22}$$

We proceed in a similar fashion to obtain an expression for the first derivative giving

$$\frac{\partial V}{\partial r} = \frac{V(r+dr_+, z) - V(r-dr_-, z)}{dr_+ + dr_-} \tag{23}$$

The infinity encountered for all points along the z-axis is dealt with by using L'Hôpital's rule

$$\lim_{r\to 0} \frac{1}{r}\frac{\partial V}{\partial r} = \frac{\partial^2 V}{\partial r^2} \tag{24}$$

The use of L'Hôpital's rule for this situation is valid because the derivatives with respect to r must vanish at the origin for a cylindrically symmetric smooth potential.

A.2. A 2-D energy conserving algorithm

A 2-D energy conserving code was devised, based on the simpler 1-D Lewis code given in [14]. For a conservative field we require that any work done against the field between two adjacent nodes is equal to the increase in potential.

$$\int_{x_0}^{x_1} \vec{F}.d\vec{x} = q\int_{x_0}^{x_1} \vec{E}.d\vec{x} = -q\big(V(\vec{x}_1) - V(\vec{x}_0)\big) \tag{25}$$

The simplest energy conserving 1-D code in [14] assumes a constant electric field between grid points, with a discontinuous electric field at the grid points themselves.

$$E(x_0) = -\frac{dV}{dx}\bigg|_{x_0} = -\frac{V(x_+) - V(x_-)}{x_+ - x_-}, \quad x_0 \in [x_-, x_+] \tag{26}$$

The work done on a particle over the interval $[x_1, x_2]$ can then be computed.

$$q\int_{x_1}^{x_2} E\, dx = -q\int_{x_1}^{x_2} \frac{V(x_+) - V(x_-)}{x_+ - x_-}\, dx$$
$$= -q\frac{V(x_+) - V(x_-)}{x_+ - x_-}(x_2 - x_1)$$
$$x_1, x_2 \in [x_-, x_+] \tag{27}$$

If a vector field equals the gradient of a scalar field, then that vector field is conservative. Both intuitively and from Eq. (27), we see

that the scalar potential can take on a linear form between each node to conserve energy.

$$V(x_0) = \frac{V(x_+) - V(x_-)}{x_+ - x_-}(x_0 - x_-) + V(x_-)$$
$$x_0 \in [x_-, x_+) \tag{28}$$

For the 2-D case, we must obtain two components of the electric field E_r and E_z at the point (r_0, z_0) using the surrounding four grid points. If we take a similar approach to the 1-D algorithm, we encounter a conceptual problem; the electric field is not constant over the cell and we cannot make it so and still satisfy Eq. (25) between all four nodes. Explicitly, using E_r for example, $V(r_+, z_+) - V(r_-, z_+) \neq V(r_+, z_-) - V(r_-, z_-)$ means that the field must be different along $z = +$ and $z = -$ axes. A solution to the conceptual problem lies with considering Eq. (28). A constant field between two grid nodes physically implies a linearly increasing potential between the two nodes. This gives us a self consistent way of computing the potential at all points along the cell boundary by using linear interpolation to define our conservative scalar field. For example, to compute $E_r(r_0, z_0)$, we linearly interpolate along z between $V(r_+, z_+)$ and $V(r_+, z_-)$ to give $V(r_+, z_0)$. We then linearly interpolate along z between $V(r_-, z_+)$ and $V(r_-, z_-)$ to give $V(r_-, z_0)$. We then do the same for E_z.

$$V(r_0, z_\pm) = \frac{V(r_+, z_\pm) - V(r_-, z_\pm)}{r_+ - r_-}(r_0 - r_-) + V(r_-, z_\pm)$$

$$V(r_\pm, z_0) = \frac{V(r_\pm, z_+) - V(r_\pm, z_-)}{z_+ - z_-}(z_0 - z_-) + V(r_\pm, z_-)$$

$$E_r(r_0, z_0) = -\frac{dV}{dr}\bigg|_{(r_0,z_0)} = -\frac{V(r_+, z_0) - V(r_-, z_0)}{r_+ - r_-}$$

$$E_z(r_0, z_0) = -\frac{dV}{dz}\bigg|_{(r_0,z_0)} = -\frac{V(r_0, z_+) - V(r_0, z_-)}{z_+ - z_-}$$

$$r_0 \in [r_-, r_+), \ z_0 \in [z_-, z_+)$$

This means that the potential takes on bilinear interpolated values between node points (though we gain little in computing those values outside of this context). This guarantees that the vector field is conservative because the electric field we compute is the gradient of this scalar field [29].

References

[1] P.T. Farnsworth, 1966, U.S. Patent No. 3,258,402.
[2] P.T. Farnsworth, 1968, U.S. Patent No. 3,386,883.
[3] R.L. Hirsch, Journal of Applied Physics 38 (1967) 4522.
[4] O. Shrier, J. Khachan, S. Bosi, M. Fitzgerald, N. Evans, Physics of Plasmas 13 (2006) 012703.
[5] J. Khachan, A. Samarian, Physics Letters A 363 (2007) 297.
[6] T.A. Thorson, R.D. Durst, R.J. Fonck, L.P. Wainwright, Physics of Plasmas 4 (1997) 4.
[7] K. Yoshikawa, et al., Nuclear Fusion 41 (2001) 717.
[8] J. Khachan, D. Moore, S. Bosi, Physics of Plasmas 10 (2003) 596.
[9] J. Khachan, S. Collis, Physics of Plasmas 8 (2001) 1299.
[10] O. Shrier, Spectroscopy and modelling of ion charge exchange in energetic discharges used in nuclear fusion, PhD thesis, University of Sydney, 2007.
[11] M. Fitzgerald, J. Khachan, S. Bosi, The European Physical Journal D – Atomic, Molecular, Optical and Plasma Physics 39 (2006) 35.
[12] J. Kipritidis, J. Khachan, M. Fitzgerald, O. Shrier, Physical Review E (Statistical, Nonlinear and Soft Matter Physics) 77 (2008) 066405.
[13] T. Sakai, K. Noborio, Y. Yamamoto, Analysis of discharge characteristics of the inertial electrostatic confinement fusion using a particle code with Monte Carlo collision scheme, in: Proceedings of the 19th IEEE/IPSS Symposium on Fusion Engineering, 19th SOFE (Cat. No. 02CH37231), IEEE, 2002, pp. 209–212.
[14] C. Birdsall, A. Langdon, Plasma Physics Via Computer Simulation, Adam Hilger, Bristol, 1991.
[15] J.P. Verboncoeur, Plasma Physics and Controlled Fusion 47 (2005) A231.
[16] H. Okuda, Journal of Computational Physics 10 (1972) 475.
[17] C. Cheng, G. Knorr, Journal of Computational Physics 22 (1976) 330.
[18] N. Baguer, Spectrochimica Acta Part B: Atomic Spectroscopy 57 (2002) 311.
[19] C. Birdsall, IEEE Transactions on Plasma Science 19 (1991) 65.
[20] M. Fitzgerald, Discharge physics and plasma transport in inertial electrostatic confinement devices, PhD thesis, University of Sydney, 2009.
[21] A.V. Phelps, Journal of Physical and Chemical Reference Data 19 (1990) 653.
[22] Y. Ralchenko, A. Kramida, J. Reader, Nist atomic spectra database (version 3.1.5), Online, 2008.
[23] P.F. Little, A. von Engel, Proceedings of the Royal Society of London, Series A, Mathematical and Physical Sciences (1934–1990) 224 (1954) 209.
[24] S.C. Brown, Basic Data of Plasma Physics, The MIT Press, Cambridge, Massachusetts, 1967.
[25] Y.P. Raizer, Gas Discharge Physics, Springer-Verlag, Berlin, Heidelberg, 1991.
[26] C.F. Barnett, et al., Atomic data for controlled fusion research (ORNL-5207), Technical report, Oak Ridge National Laboratory, 1977.
[27] W. Eckstein, H. Verbeek, Journal of Nuclear Materials 76–77 (1978) 365.
[28] F. Assous, T. Pougeard Dulimbert, J. Segré, Journal of Computational Physics 187 (2003) 550.
[29] A.B. Langdon, Journal of Computational Physics 12 (1973) 247.
[30] G.A. Cottrell, Journal of Physics E: Scientific Instruments 15 (1982) 432.
[31] I. Langmuir, Physical Review 2 (1913) 450.
[32] E. Kreyszig, Advanced Engineering Mathematics, 8th ed., John Wiley, New York, 1999.